

Efficient Polycrystalline Single-Cation Perovskite Light-Emitting Diodes by Simultaneous Intracrystal and Interfacial Defect Passivation

Hobeom Kim, Jung-Min Heo, Christoph Wolf, Young-Hoon Kim, Seong-Chul Lee, Eojin Yoon, Geon-Hui Lee, Kyung Yeon Jang, Junmo Park, Joo Sung Kim, Min-Ho Park, Su-Hun Jeong, Himchan Cho, Tae-Hee Han, Emad Oveisi, Mohammad Khaja Nazeeruddin, and Tae-Woo Lee*

Polycrystalline perovskite light-emitting diodes (PeLEDs) have shown great promise with high efficiency and easy processability. However, PeLEDs using single-cation polycrystalline perovskite emitters have demonstrated low efficiency due to defects within the grains and at the interfaces between the perovskite layer and the charge injection contact. Thus, simultaneous defect engineering of perovskites to suppress exciton loss within the grains and at the interfaces is crucial for achieving high efficiency in PeLEDs. Here, 1,8-octanedithiol which is a strong nucleophile, is used to increase the luminescence efficiency of a single-cation perovskite by suppressing non-radiative recombination within the grains of their polycrystalline emitter film as well as at their interface with an anode. The dithiol additive performs a multifunctional role in defect passivation, spatial confinement of excitons, and prevention of exciton quenching at the interface between the perovskite layer and the underlying hole-injection layer. Photoluminescence studies demonstrate that incorporating the dithiol additive significantly enhances the charge carrier dynamics in perovskites, resulting in an external quantum efficiency (EQE) of up to 23.46% even in a simplified PeLED that does not use a hole-injection layer. This represents the highest level of EQE achieved among devices utilizing polycrystalline single-cation perovskites.

1. Introduction

Perovskite light-emitting diodes (PeLEDs) have become the focus of interest based on promising properties of the perovskites as a light emitter such as high brightness, high color purity, and facile color tunability.^[1–7] Also, excellent optoelectronic properties of perovskites based on high defect tolerance enabled their efficient radiative recombination and high luminous efficiency.^[2,8] Thus, PeLEDs have achieved external quantum efficiency (EQE) of over 20% in green,^[1,9–11] red,^[12–14] and infra-red.^[15–18] Nevertheless, defect-induced traps in perovskites can still prevent efficient radiative recombination and limit device characteristics of PeLEDs in terms of efficiency and stability.^[19–23] Due to the ionic nature of the defects, their influence on recombination dynamics and structural stability of perovskites becomes more significant under an electric field.^[24,25] To be specific, the ions can accumulate at the interface of perovskites

H. Kim, J.-M. Heo, C. Wolf, Y.-H. Kim, E. Yoon, K. Y. Jang, J. S. Kim, M.-H. Park, S.-H. Jeong, H. Cho, T.-H. Han, T.-W. Lee
Department of Materials Science and Engineering
Seoul National University
1 Gwanak-ro, Seoul 08826, Republic of Korea
E-mail: twlees@snu.ac.kr

H. Kim, J. Park
School of Materials Science and Engineering
Gwangju Institute of Science and Technology (GIST)
123 Cheomdangwagi-ro, Gwangju 61005, Republic of Korea

 The ORCID identification number(s) for the author(s) of this article can be found under <https://doi.org/10.1002/smll.202405272>

© 2024 The Author(s). Small published by Wiley-VCH GmbH. This is an open access article under the terms of the [Creative Commons Attribution-NonCommercial-NoDerivs](https://creativecommons.org/licenses/by/4.0/) License, which permits use and distribution in any medium, provided the original work is properly cited, the use is non-commercial and no modifications or adaptations are made.

DOI: 10.1002/smll.202405272

S.-C. Lee
PEROLED Co. Ltd.
Building 940, 1 Gwanak-ro, Seoul 08826, Republic of Korea
S.-C. Lee, T.-W. Lee
Institute of Engineering Research
Soft Foundry
Seoul National University
1 Gwanak-ro, Seoul 08826, Republic of Korea

G.-H. Lee
Department of Materials Science and Engineering
Pohang University of Science and Technology (POSTECH)
77 Cheongam-ro, Pohang 37673, Republic of Korea

E. Oveisi
Interdisciplinary Centre for Electron Microscopy (CIME)
École Polytechnique Fédérale de Lausanne (EPFL)
Lausanne CH-1015, Switzerland

M. K. Nazeeruddin
Institute of Chemical Sciences and Engineering
École Polytechnique Fédérale de Lausanne (EPFL)
Lausanne CH-1015, Switzerland

with an adjacent layer, in particular, a hole-injection layer (HIL) during the operation of PeLEDs as the negatively charged halide ion is the dominant defect within perovskites.^[26,27] Therefore, charge trapping and quenching via non-radiative recombination can occur more easily at the interface with the HIL.^[24,28] Also, the accumulated ions can aggravate the operational stability of PeLEDs by increasing a local electric field at the interface.^[28] Therefore, defect passivation of perovskites and suppression of non-radiative recombination inside grains and at the interface between the perovskite layer and the charge injection contacts with perovskites are essential to the demonstration of high-efficiency PeLEDs.

Polycrystalline single-cation PeLEDs have shown low EQE even though they can be processed much easier than multi-cation perovskites, which can be ascribed to lacking strategy on defect passivation in the emitting layer and reducing exciton quenching at the interface in the devices. Various strategies of defect passivation have been reported to mitigate the negative impact of defects on the charge carrier dynamics of perovskites.^[29–31] The majority of them are based on Lewis-base passivation of under-coordinated Pb^{2+} that is correlated with the halide vacancy.^[20] The molecules including nitrogen, sulfur, oxygen or phosphorus which can donate lone pair electrons have exhibited effective passivation of the under-coordinated Pb^{2+} by neutralizing the perovskite lattice.^[24,32–34] Thus, it can prevent undesirable non-radiative recombination at the corresponding trap sites. In addition to defect passivation, preventing exciton quenching at the interface between the perovskite and a conducting polymer hole-injection layer is also important. A surface-enriched perfluorinated ionomer (PFI) layer on a self-organized hole-injection layer (Buf-HIL), composed of poly(3,4-ethylenedioxythiophene) polystyrene sulfonate (PEDOT: PSS) and PFI, was proven to be useful for blocking exciton quenching at the interface.^[35]

In this study, we introduce a dithiol reagent, 1,8-octanedithiol (ODT), into polycrystalline single-cation perovskite for comprehensive suppression of non-radiative recombination inside grains and at the interface between the perovskite and a conducting polymer HIL, which resulted in high efficiency in the PeLED with a simplified device structure. This suppression is achieved through ODT's multifunctional role in defect passivation of the perovskite, spatial confinement of excitons in small nanograins, and reduction of exciton quenching at the hole injection interface (**Figure 1**). The nucleophilic dithiol can be particularly useful for Lewis-base passivation of under-coordinated Pb^{2+} in methylammonium lead bromide (MAPbBr_3). Also, the additive can surround perovskite grains where excitons can be

spatially confined inside the grains. Furthermore, due to the distribution of the additive dominantly at the lower part of the perovskite layer, exciton quenching at the interface between the perovskite and the underlying HIL can be reduced. Enhanced carrier dynamics of the perovskites with the additive are revealed by photoluminescence (PL) studies. As a result, PeLEDs using the ODT-incorporated polycrystalline MAPbBr_3 exhibited a high EQE of 23.46% even in a simplified structure with a conducting polymer anode (CPA)/perovskite/TPBi/cathode configuration without using a HIL. This represents the highest level of EQE achieved by PeLEDs using polycrystalline single-cation perovskite emitters (Table S1 and Figure S1, Supporting Information).

2. Results and Discussion

We used 10 vol % of ODT in the MAPbBr_3 precursor solution, and we performed liquid-state ^1H nuclear magnetic resonance (NMR) spectroscopy of the solution in comparison to the pristine MAPbBr_3 and ODT per se to investigate the underlying chemistry in the precursor state (**Figure 2a**). The solutions for the NMR spectroscopy were prepared in dimethyl sulfoxide- d_6 ($\text{DMSO}-d_6$) to keep the chemical environment and concentration the same as for the actual film fabrication. The spectrum of pristine MAPbBr_3 exhibited two dominant proton signals at $\delta = 7.53$ and 2.37 ppm that represent the ammonium ($-\text{NH}_3^+$) and the methyl ($-\text{CH}_3$) group of methylammonium (MA), respectively. On the other hand, the spectrum of ODT showed discrete peaks as denoted from *a* to *e* according to the position of the protons within the molecule. The addition of ODT to the pristine MAPbBr_3 solution caused a broadening of the proton signal of the ammonium group (denoted as *g*) due to the increasing acidity of the solution (Figure S2, Supporting Information).^[36] Also, the proton signals by ODT itself arose. However, the proton signal of the thiol group (indicated as *a*) exhibited a downfield shift from 2.154 to 2.158 ppm indicating deshielding of the thiol moiety whereas the rest of the proton signals of CH_2 within ODT resulted in an upfield shift (Figure S3, Supporting Information). We may attribute the deshielding to Lewis base-acid interaction between the thiol and Pb^{2+} based on a strong nucleophilicity of the thiol group. In contrast, this deshielding effect on the thiol proton can result in a redistribution of electron density within the ODT molecule. As Pb^{2+} withdraws electron density from the thiol group, the electron density around the adjacent $-\text{CH}_2$ groups may increase relative to the thiol group, resulting in relative shielding and an upfield shift. Despite the small magnitude of the shifts, the observed changes are consistent with the corresponding chemical interactions.

The MAPbBr_3 films were prepared by spin-coating with the nanocrystal pinning (NCP) process using TPBi in chloroform.^[19,37] The presence of ODT in the precursor led to the formation of smaller grains of MAPbBr_3 that can be more favorable to the spatial confinement of excitons than the pristine MAPbBr_3 (Figure S4, Supporting Information).^[9,38] This grain size reduction can be explained using the Kubota-Mullin model, which describes how the addition of an additive, such as ODT, can increase the nucleation rate during crystallization.^[39] According to the model, the increased nucleation rate leads to a higher density of nucleation sites, resulting in smaller, more uniform grains. Additionally, during the crystallization

T.-W. Lee
Research Institute of Advanced Materials
Seoul National University
1 Gwanak-ro, Seoul 08826, Republic of Korea
T.-W. Lee
School of Chemical and Biological Engineering
Seoul National University
1 Gwanak-ro, Seoul 08826, Republic of Korea
T.-W. Lee
SN Display Co. Ltd.
Building 33, 1 Gwanak-ro, Seoul 08826, Republic of Korea

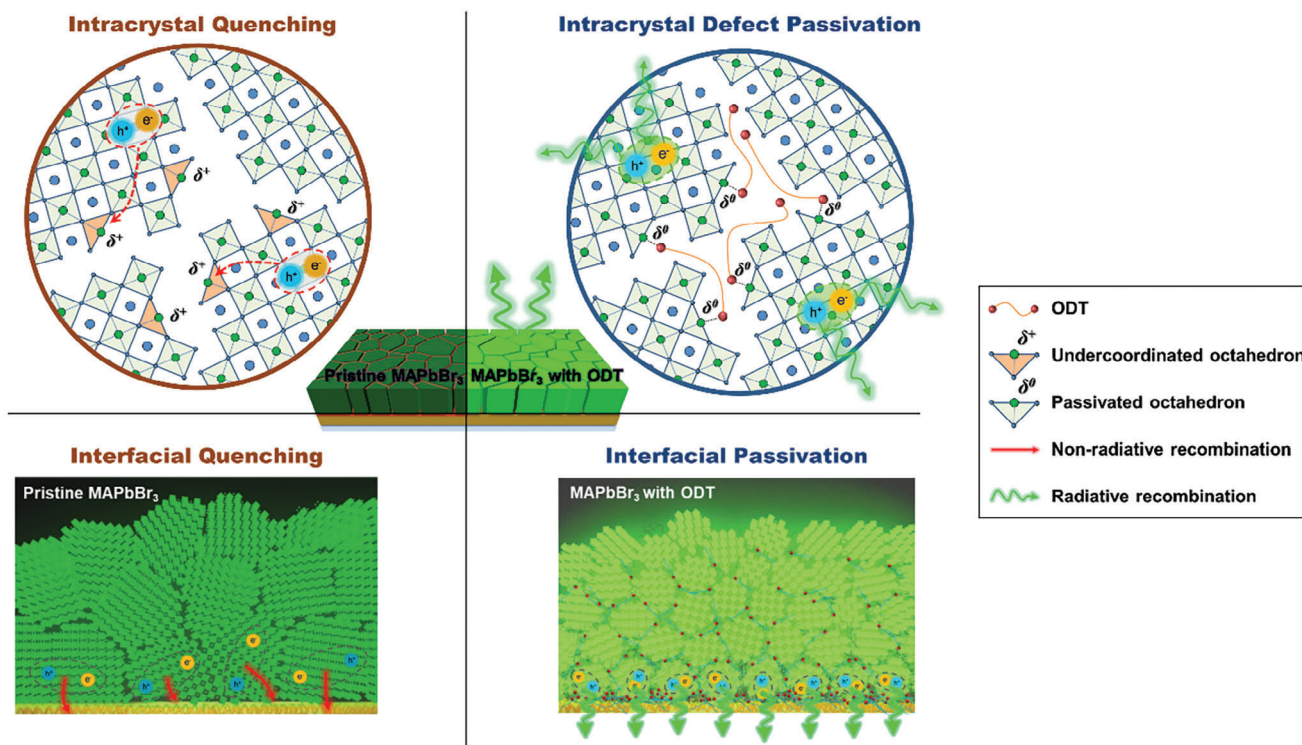


Figure 1. Schematic illustration of defect passivation, spatial confinement of excitons, and prevention of exciton quenching at the interface by the introduction of ODT. Non-radiative recombination of excitons by under-coordinated Pb^{2+} in pristine MAPbBr_3 (upper left) and Lewis-base passivation of the defect by ODT that also spatially confines excitons inside grains to neutralize the defect sites and contribute to efficient radiative recombination (upper right). The film without ODT is subject to non-radiative recombination at the interface (lower left) whereas the use of ODT facilitates radiative recombination as it prevents exciton quenching at the interface of perovskite/HIL (lower right).

process of MAPbBr_3 , ODT may interact with the growing crystal facets, potentially hindering their growth and further promoting the formation of smaller grains. These smaller grains may contribute to the improved spatial confinement of excitons. Dynamic secondary ion mass spectrometry (DSIMS) depth profile of the ODT-incorporated MAPbBr_3 film revealed an increase in the sulfur intensity toward the substrate side, indicating the dominant ODT distribution at the bottom region of the film (Figure 2b). In contrast, a negligible sulfur signal was observed in the pristine perovskite film. High-angle annular dark-field scanning transmission electron microscopy (HAADF-STEM) corroborated the distribution of ODT within the film. Figure 2c shows a cross-sectional view of the interface region from the HIL to the perovskite layer and we observed a discernible contrast among the areas as indicated in the red boxes; areas #1, #2, and #3 illustrate a region of MAPbBr_3 , the ODT compound, and the HIL, respectively. The integrated energy-dispersive X-ray spectroscopy (EDX) spectrum of each area represents the presence of peaks for Pb and S in the three areas (Figure 2d). Given the similar intensity of Pb-M β between areas #1 and #2, we can assign those areas to the perovskite layer. Notably, the dominant peak of the area #2 spectrum exhibited a shift to lower energy, which can be attributed to the inclusion of the sulfur-containing ODT in the area. In contrast, the spectrum of area #3 showed a reduction of Pb-M β intensity while its major peak chiefly arose from an increasing intensity of S-K due to PEDOT: PSS.

Thus, based on the results of DSIMS and STEM-EDXS analyses, we may conclude that the ODT is dominantly distributed at the bottom region of the perovskite layer at its interface with the HIL. Despite the incorporation of ODT in the perovskite layer, X-ray diffraction (XRD) of the film did not show a significant change in its pattern from that of pristine perovskite film (Figure S5, Supporting Information). This indicates that the addition of ODT did not deform the crystalline structure of MAPbBr_3 . Instead, it is more likely that the ODT compound surrounds the grains and occupies the grain boundary, which may enable excitons to be well confined inside the grains.

We performed various PL characterizations of the developed films to investigate the effects of the ODT. The 10% ODT-incorporated MAPbBr_3 film exhibited a higher steady-state PL intensity than pristine MAPbBr_3 film (Figure 3a,b). The intensity difference was more pronounced when the films were excited from the substrate side compared to the top of the film. This trend was consistent with 7% ODT incorporation, but a 13% addition resulted in a decrease in PL intensity likely due to the degradation of the crystallinity and homogeneity of the perovskite emitter (Figure S6, Supporting Information). Additionally, we observed a noticeable reduction in FWHM values when ODT was incorporated into MAPbBr_3 (Figure S7, Supporting Information). When excited from the substrate side, the FWHM decreased by 1.4 nm, from 24.0 to 22.6 nm, whereas excitation from the film side resulted in a smaller reduction of 0.7 nm, from 27.4 to 26.7 nm. The noticeable intensity difference and pronounced

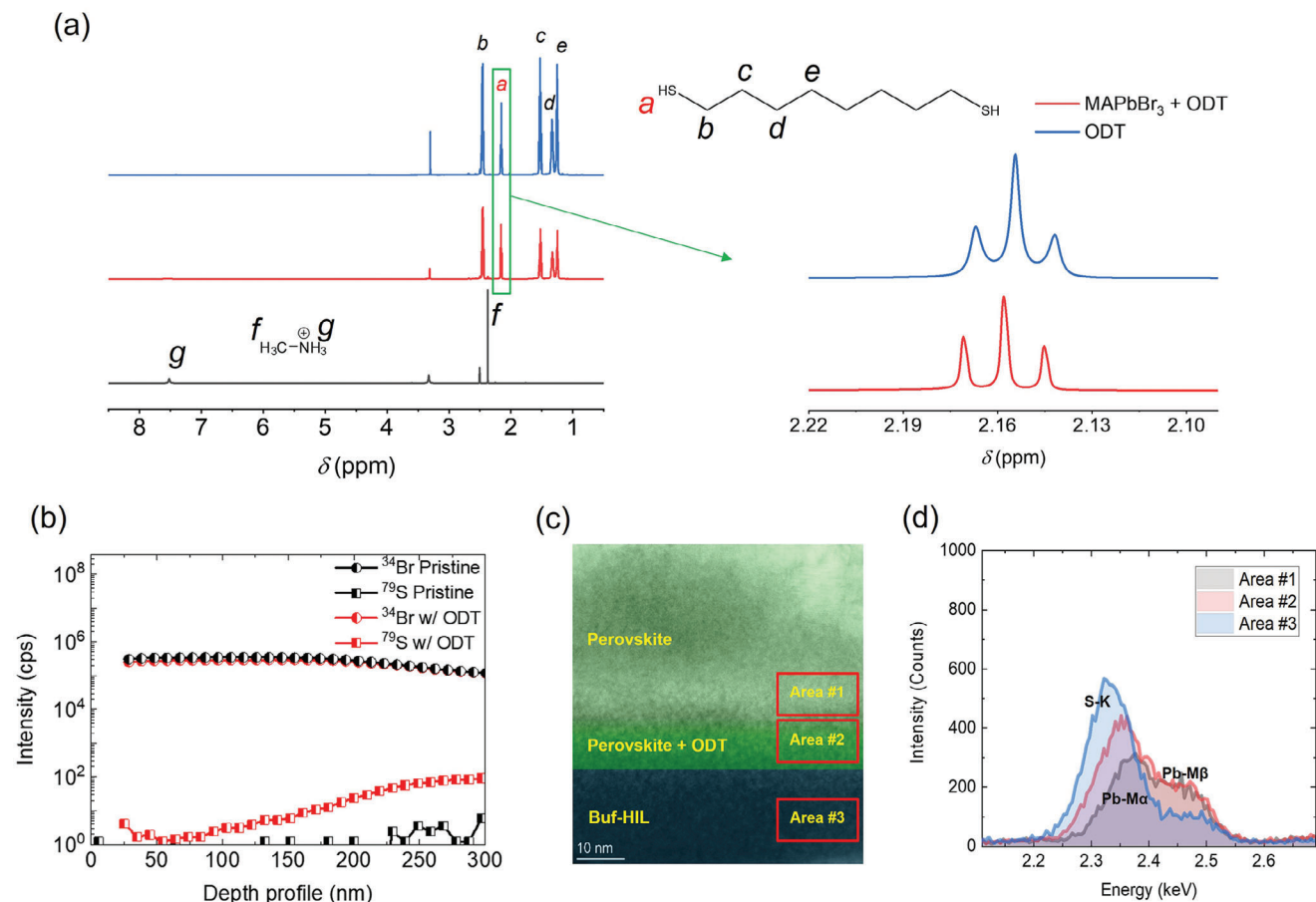


Figure 2. a) ^1H NMR spectra of MAPbBr_3 (black), MAPbBr_3 with ODT (10 vol%) (red) in $\text{DMSO}-d_6$, and pure ODT (blue). b) DSIMS depth profile of perovskite films. Distributions of S and Br in MAPbBr_3 (black) and MAPbBr_3 with ODT (red). c) HAADF scanning STEM cross-section image of ODT-incorporated perovskite film. d) Integrated EDX spectra of the acquired data from the red-boxed areas in (c).

narrowing of the FWHM upon substrate-side excitation suggests that defect passivation by ODT is more effective at the bottom interface of the perovskite layer, thereby reducing defect-related non-radiative recombination. This behavior aligns with the predominant distribution of the ODT within the film as characterized by the DSIMS and HAADF-STEM above. We also performed transient PL measurements using time-correlated single-photon counting (TCSPC) (Figure 3c). The PL decay curves were fitted to the bi-exponential decay function, $\gamma = A_1 e^{-t/\tau_1} + A_2 e^{-t/\tau_2}$ where τ_1 and τ_2 are the lifetimes for the fast and slow decays, respectively. The ODT-incorporated perovskite exhibited a significant increase in PL average lifetime ($\tau_{\text{Ave}} = 185.82 \text{ ns}$) compared to that of the pristine film ($\tau_{\text{Ave}} = 105.98 \text{ ns}$). The detailed decay parameters are summarized in Table S2 (Supporting Information). The enhanced PL characteristics of the ODT-incorporated perovskite can be attributed to the comprehensively suppressed non-radiative recombination based on the multi-contribution of the ODT compound. 1) Under-coordinated Pb^{2+} formed by bromide vacancy (V_{Br}^+) on the grain boundary of MAPbBr_3 can be passivated by Lewis-base ODT to neutralize the lattice and subsequently annihilate corresponding defect states.^[40] 2) The insulating ODT compound that surrounds the grains can spatially confine excitons inside the grains suppressing their quenching

at the grain boundary.^[41] Given the distribution profile of ODT and the difference in the steady-state PL intensity according to the direction of light illumination, the defect passivation, and the spatial confinement can be dominantly effective at the lower part of the perovskite layer. 3) Furthermore, the ODT compound distributed at the bottom region of the perovskite layer can act as an additional buffer layer on the self-organized conducting polymer (PEDOT:PSS: PFI) to block exciton quenching at their interface. We further investigated the passivation effect of ODT by spin-coating it on the top surface of MAPbBr_3 films. A 0.3 vol% of ODT solution in chloroform was spin-coated at 3000 rpm for 30 s. The ODT surface passivation led to a significant increase in PL intensity when excited from the film side, while the increase was less pronounced when excited from the substrate side (Figure S8, Supporting Information). This result further supports the effectiveness of ODT passivation.

Analysis of temperature-dependent integrated PL intensity of the films gives more specific information about recombination dynamics (Figure 4a; Figure S9, Supporting Information).^[42] The intensity curves were fitted to an Arrhenius formula

$$I(T) = \frac{I_0}{1 + A e^{-E_a/(k_B T)}} \quad (1)$$

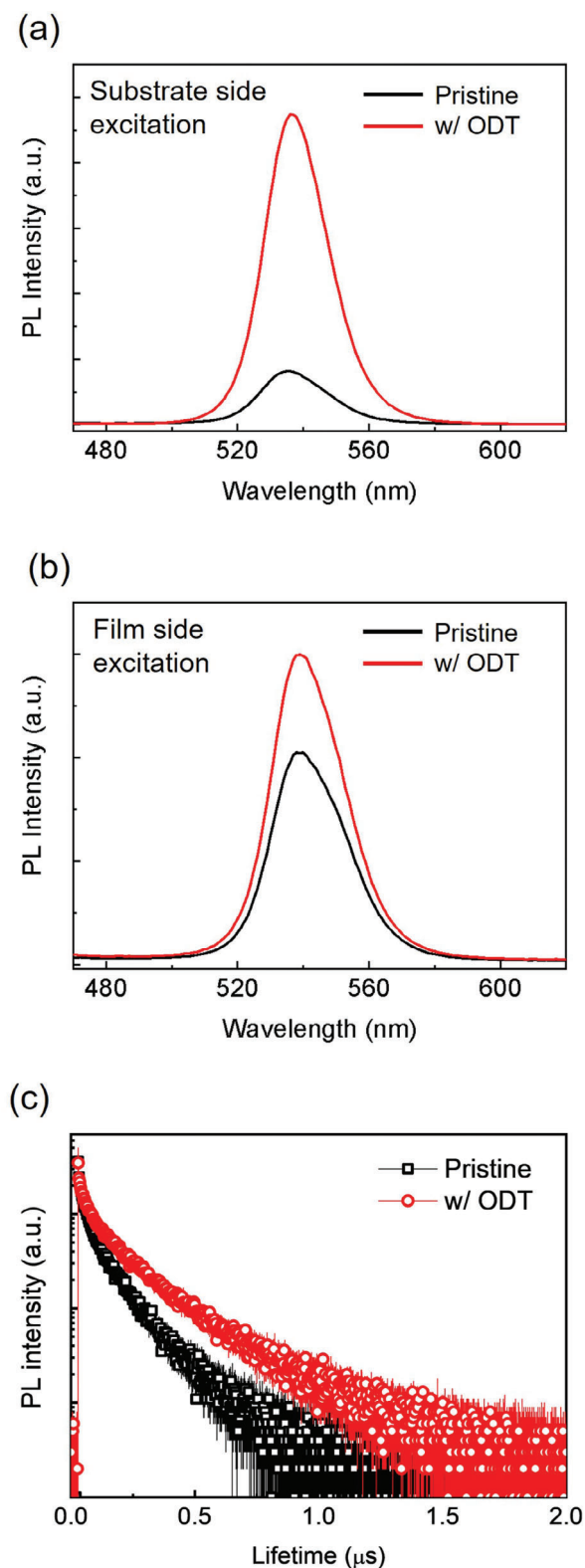


Figure 3. Steady-state PL spectrum of ODT-incorporated MAPbBr₃ (red) and pristine MAPbBr₃ (black) excited a) from the substrate side and b) from the film side. c) Transient PL decay curves of the films.

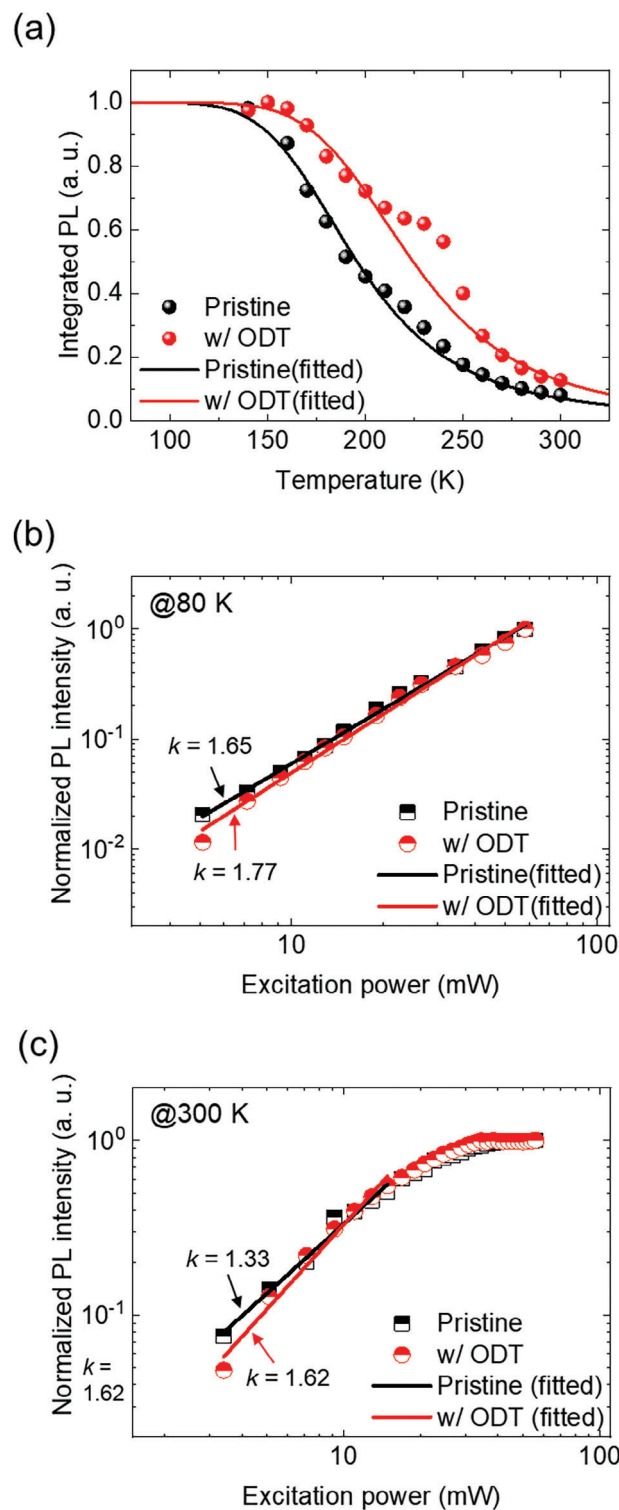


Figure 4. a) Temperature-dependent integrated PL intensity of pristine and ODT-incorporated MAPbBr₃ films. Solid lines are fit to the data using the Arrhenius equation. Excitation-power dependent normalized PL intensity at b) 80 K and c) 300 K. Solid lines are linear fits to the data with a power-law k .

where $I(T)$ is the integrated PL intensity as a function of temperature T , I_0 is $I(T)$ at $T = 0$, and K_B is the Boltzmann constant. E_a is the activation energy for the effective thermal activation process that leads to non-radiative recombination. By fitting the curves, we obtained $E_a = 236.2 \pm 7.0$ meV for the ODT-incorporated MAPbBr₃, and $E_a = 128.0 \pm 3.6$ meV for the pristine MAPbBr₃; the difference indicates that the occurrence of non-radiative recombination demands much higher energy in the ODT-incorporated MAPbBr₃ because the ODT compound globally contributed to the defect passivation, spatial confinement of exciton, and prevention of exciton-quenching at the interface, which facilitated radiative recombination. The effect of ODT was also investigated by analysis of excitation-power-dependent PL intensity (I) of the perovskite films at 80 and 300 K (Figure 4b,c; Figure S10, Supporting Information). As the PL of perovskite is dominated by near-band-edge emission, its intensity (I) follows a power-law dependence on excitation power (P) as $I = P^k$ and recombination processes can be assorted according to the k values;^[43] Free- and bound-exciton radiative recombination has $1 < k < 2$, and a donor or an acceptor level-mediated recombination has $k < 1$. In other words, a lower k accounts for a higher density of trap states. At 80 K, the ODT-incorporated MAPbBr₃ had $k = 1.77 \pm 0.05$, and pristine MAPbBr₃ had $k = 1.65 \pm 0.02$. For both perovskites, thus, free- and bound-exciton radiative recombination were dominant for emission, but the slightly higher k of the ODT-incorporated MAPbBr₃ accounts for a lower density of trap states due to the defect passivation. Although both curves showed a change in the power-law at 300 K as increasing the excitation power, the ODT-incorporated MAPbBr₃ had $k = 1.62 \pm 0.10$ and the pristine MAPbBr₃ had 1.33 ± 0.08 where the power-law was maintained constant ($P < \approx 15$ mW). The power law in both films was lower than that at 80 K as more trap states can be thermally activated at 300 K. Nevertheless, the smaller reduction of k with the employment of the ODT can be indicative of a lower trap density by defect passivation than the pristine film. The saturation of both curves with the increase in P can be attributed to the trap filling.^[44]

We used the pristine and the ODT-incorporated MAPbBr₃ films as an emitter of PeLEDs. The device structure was FTO/Buf-HIL (50 nm)/perovskite (400 nm)/TPBi (50 nm)/LiF (1 nm)/Al (100 nm). Although ODT is non-conductive, its effective defect passivation may compensate for any potential reduction in device current, allowing the current density to remain on par with that of the control device using pristine MAPbBr₃. The device using the ODT-incorporated MAPbBr₃ exhibited significantly improved luminescence characteristics (maximum luminance $L_{\max} = 21,757$ cd m⁻² and maximum current efficiency $CE_{\max} = 39.11$ cd A⁻¹) compared to the device using the pristine MAPbBr₃ ($L_{\max} = 14,183$ cd m⁻² and $CE_{\max} = 23.41$ cd A⁻¹) (Figure 5a–c). The device with the ODT-incorporated MAPbBr₃ achieved a maximum EQE of 7.87% which was 46.0% higher than that of the device with the pristine MAPbBr₃ (5.39%) (Figure 5d). Histogram of EQE of the devices exhibited clear superiority of the ODT-incorporated perovskites over the pristine perovskites (Figure S11, Supporting Information). Both devices showed peak electroluminescence (EL) emission at 541 nm (Figure S12, Supporting Information). The improvement in the EL characteristics can be attributed to the comprehensive suppression of non-radiative recombination by passivation of the

under-coordinated Pb²⁺, spatial confinement of exciton, and exciton quenching blocking at the interface by the ODT compound. Furthermore, we demonstrated PeLEDs that have a simplified device structure based on CPA (Figure 6a).^[45] The device using pristine MAPbBr₃ exhibited a CE_{\max} of 60.74 cd A⁻¹ and an EQE of 13.01% while the device using ODT-incorporated MAPbBr₃ achieved a CE_{\max} of 111.30 cd A⁻¹ and the highest EQE of 23.46% among PeLEDs employing single-cation polycrystalline perovskite emitters (Figure 6b–e; Table S1, Supporting Information). Although the devices based on the CPA exhibited lower current density compared to those using FTO/Buf-HIL due to the CPA's lower conductivity, the simplified device structure—free from the anode/HIL interface—minimizes carrier losses, avoids the formation of a charge injection barrier between the anode and HIL, and mitigates exciton quenching due to the surface enriched PFI layer. These factors contribute to superior luminescence characteristics compared to the FTO-based devices. The absence of metal oxide electrodes (e.g., ITO and FTO) eliminates the potential for metallic species (e.g., In and Sn) generation, which can migrate into overlying layers and cause exciton quenching. Consequently, this contributes to the better performance of the CPA-based devices with more efficient radiative recombination than the FTO-based devices. Statistics of EQE and CE_{\max} of the devices exhibited that the ODT incorporation leads to higher luminescence efficiency of the devices (Figure S13, Supporting Information).

Furthermore, the PeLEDs using the ODT-incorporated MAPbBr₃ emitter demonstrated better operational stability than the control device under a constant current to elicit an initial luminance of 100 cd m⁻² (Figure 6f). The ODT-incorporated PeLED exhibited a significantly extended operational lifetime ($T_{50} = 139$ min) compared to the pristine PeLED ($T_{50} = 59$ min). We attribute this improvement in device stability to the ODT compound, which likely enhances the material stability of the perovskite through defect passivation. Additionally, the ODT compound distributed at the interface may act as a buffer layer, alleviating potential degradation caused by ionic defect accumulation at the interface.

3. Conclusion

In conclusion, we used a multifunctional dithiol-based additive, ODT to increase the luminescence efficiency of polycrystalline PeLEDs via comprehensive suppression of non-radiative recombination by defect passivation of polycrystalline perovskites inside nanograins, and reduction of interfacial exciton quenching between the perovskite layer and the underlying HIL. Under-coordinated Pb²⁺ in MAPbBr₃ was passivated by the Lewis-base ODT that can neutralize the defect and annihilate the corresponding defect states. Also, excitons can be spatially confined inside the grains by the ODT compound that surrounds the grains. Moreover, exciton quenching at the interface between the perovskite layer and the underlying HIL was inhibited due to the presence of the abundant ODT compound that might act as an additional buffer layer suppressing non-radiative recombination. Thus, the enhanced recombination dynamics by using the ODT compound in MAPbBr₃ were revealed by various PL studies and the demonstration of PeLEDs. Finally, the combinatorial use of the ODT and CPA achieved a high EQE (23.46%) in single-cation

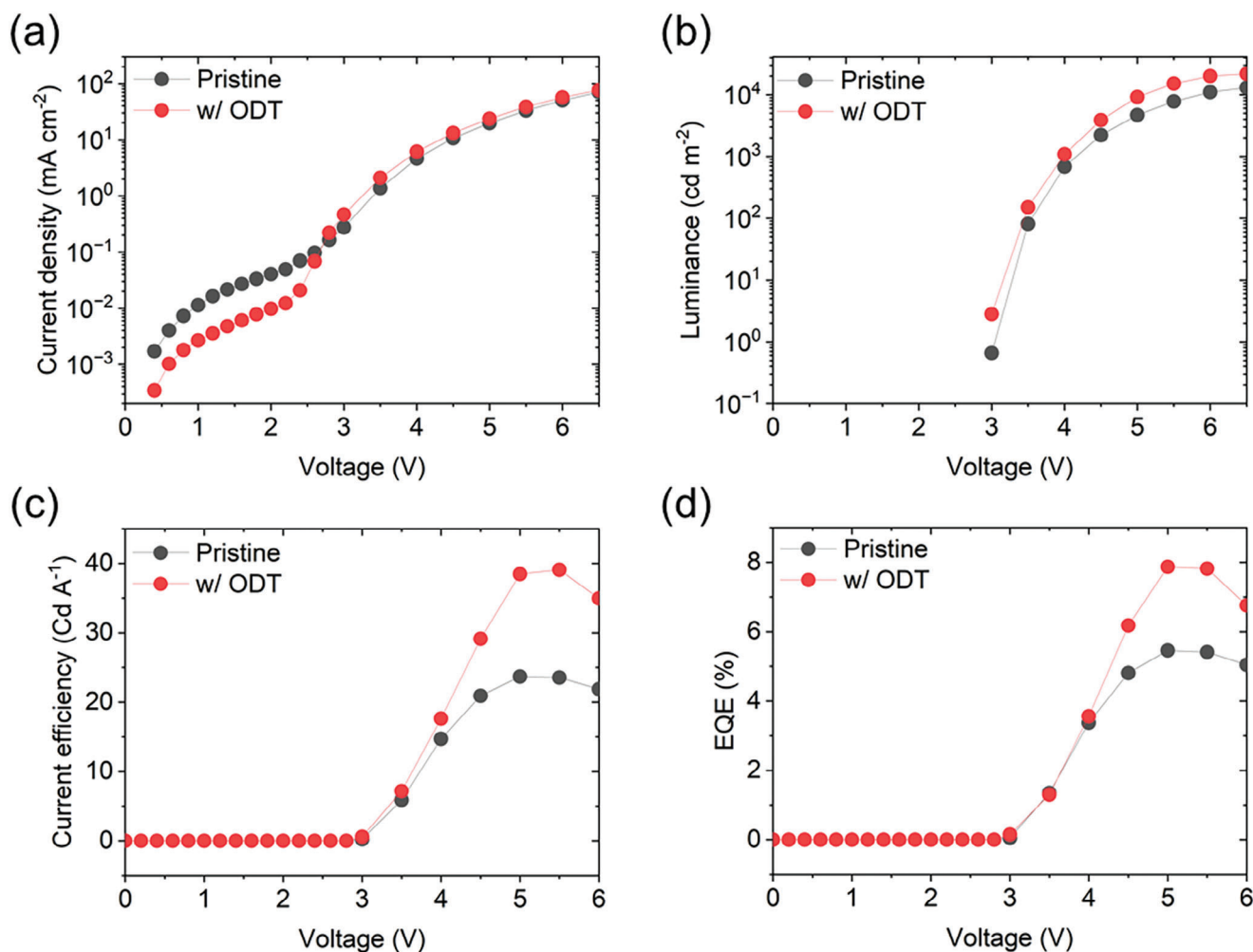


Figure 5. a) Current density, b) luminance, c) current efficiency, and d) EQE of PeLEDs using pristine or ODT-incorporated MAPbBr₃ based on FTO anode as a function of applied voltage.

PeLEDs even with a simplified device structure, and it proves that the simple molecular additive approach within polycrystalline perovskites is also highly promising in terms of the achievement of high-efficiency single-cation PeLEDs. Thus, we further suggest the use of nucleophilic thiol compounds for various perovskites to exploit its intriguing versatile capability that leads to comprehensive suppression of non-radiative recombination in the community of PeLEDs.

4. Experimental Section

Preparation of Perovskite Solutions: CH₃NH₃Br (MABr) (Dyesol) and PbBr₂ (Aldrich) (1.08:1 molar ratio) were dissolved (1.2 M) in dimethyl sulfoxide (DMSO) (Aldrich). For the incorporation of dithiol, 10 vol % of 1,8-octanedithiol (ODT) (Aldrich) was added to the MAPbBr₃ precursor solution, and the solution was vigorously stirred.

PeLEDs Fabrication: Fluorine-doped tin oxide (FTO) coated glass substrates were used after cleaning by sonication with acetone and isopropanol. The Buf-HIL layer was spin-coated on the substrates at 3000 rpm for 90 s and annealed on a hot plate for 30 min at 150 °C in air. Buf-HIL solution was composed of PEDOT: PSS (Clevis P VP AI4083) and tetrafluoroethylene-perfluoro-3,6-dioxa-4-methyl-

7-octene-sulfonic acid copolymer (PFI) (Sigma–Aldrich) (1:1 wt:wt). For simplified PeLEDs, instead of FTO/Buf-HIL, a 100-nm-thick self-organized conducting polymer anode (CPA) was spin-coated. The CPA consists of poly(3,4-ethylenedioxythiophene): poly(styrenesulfonate) (PEDOT: PSS) (Clevis PH500), perfluorinated ionomer, tetrafluoroethylene-perfluoro-3,6-dioxa-4-methyl-7-octenesulfonic acid copolymer (PFI) (PEDOT:PSS: PFI = 1:2.5:11.2 (w:w:w)), and a small amount of DMSO additive. Further details about the Buf-HIL and CPA, such as work function, sheet resistance, and conductivity, can be found in the previous work.^[45] The spin-coated CPA films were annealed at 200 °C for 10 min in ambient. Subsequently, the perovskite films were deposited by spin-coating the precursor solutions in a nitrogen-filled glove box. During the spin-coating, the NCP process was applied by using TPBi solution in chloroform (0.1 wt.%). The perovskite films were annealed at 90 °C for 10 min, then the samples were loaded into a high-vacuum chamber (< 10⁻⁷ Torr) and then TPBi (50 nm), LiF (1 nm), and Al (100 nm) were thermally evaporated as an electron transport layer, injection layer, and cathode layer, respectively. The devices were encapsulated by a glass lid using UV-curable resin.

Device Characterization: All the devices were measured after encapsulation in the N₂ atmosphere. The current-voltage-luminance characteristics of PeLEDs were measured as described in the previous work using a computer-controlled source-measurement unit (Keithley 236) and a spectroradiometer (Minolta CS2000).^[46]

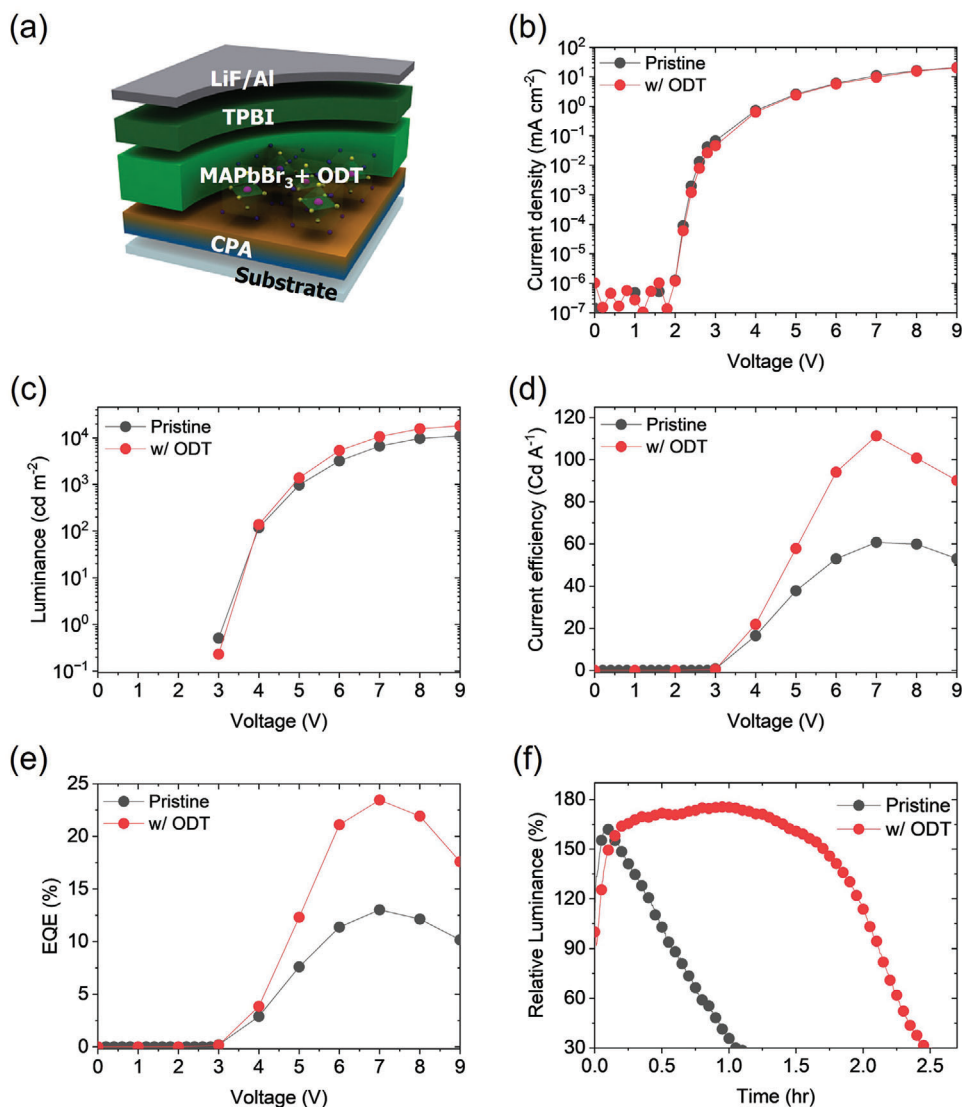


Figure 6. a) Device structure of a simplified PeLED based on conducting polymer anode (CPA). b) Current density, c) luminance, d) current efficiency, e) EQE, and f) relative luminance over time of the device based on the CPA using pristine and ODT-incorporated MAPbBr₃.

¹H NMR Measurement: A high-resolution NMR spectrometer (Bruker Advance 600 MHz) was used to obtain the ¹H NMR spectra. For the pristine perovskite precursor, MABr and PbBr₂ were dissolved in DMSO-*d*₆ (0.02 M) and the ODT-added precursor solution was prepared by adding 10 vol% of ODT in the pristine solution. Pristine ODT was also prepared at the same concentration as the perovskite solution in DMSO-*d*₆ for comparison. All the samples were prepared at room temperature in an N₂ atmosphere and measured at room temperature.

Steady-State PL Measurement: The steady-state PL of MAPbBr₃ layers on Glass/CPA was measured using a spectrofluorometer (JASCO FP8500).

Time-Correlated Single-Photon Counting Measurement: The PL decay of MAPbBr₃ films on glass/CPA was investigated using a TCSPC system. A pulsed diode-laser head (PicoQuant, LDH-D-C-405) coupled with a laser-diode driver (PicoQuant, PDL 800-D) was used as an excitation source. The fluorescence was spectrally resolved using a monochromator (Acton, SP-2155) and its time-resolved signal was measured by a TCSPC module (PicoQuant, PicoHarp) equipped with a microchannel plate photomultiplier tube (Hamamatsu, MCP-PMT, R3809U-50). The PL decay was measured at 545 nm. To calculate the flu-

orescence lifetime from the actual decay signal, the output curve was deconvoluted using FluoFit (PicoQuant).

Temperature- and Excitation Power-Dependent PL Measurement: The temperature of the samples was controlled by a liquid-nitrogen cryostat (Oxford instruments DN2, sample in exchange gas) using Oxford instruments Mercury iTC. The sample temperature was read from a single sensor and was believed to be accurate within 1K according to manufacturer specifications. As an excitation light source, a 405 nm continuous-wave laser diode (PicoQuant, LDH-D-C-405) was used and the emitted light was collected using a fiber-coupled stellarNet blue-wave spectrometer. The laser power was varied using a laserdriver (PicoQuant, PDL 800-D) from 3 to 58 mW which was confirmed by a laser power meter (Thorlabs, PM100D).

Transmission Electron Microscopy (STEM): Lamella for STEM-EDX analysis was prepared by conventionally focused ion beam lift-out using a Zeiss NVision40. High-angle annular dark-field (HAADF) STEM imaging and energy dispersive X-ray spectroscopy (EDXS) were performed on a Thermo Fisher Titan-Themis 60–300, equipped with a high brightness Schottky X-FEG gun, four silicon drift Super-X EDX detectors, and

Velox acquisition software. EDX data were collected in the form of spectrum images, in which a focused electron probe was scanned in raster (1024 × 1024 pixels) across a region of interest in the scanning TEM (STEM) mode. For each scan point, structural information was obtained from the electron scattering incident on a high-angle annular dark-field detector, and simultaneously, an EDX spectrum was obtained by collecting X-rays emitted from the local volume probed by the electron beam. Spectrum images were acquired with a probe current of ≈250 pA at an acceleration voltage of 200 kV.

Supporting Information

Supporting Information is available from the Wiley Online Library or from the author.

Acknowledgements

This work was supported by the National Research Foundation of Korea (NRF) grant funded by the Korean government (Ministry of Science, ICT & Future Planning) (NRF-2016R1A3B1908431). M.K.N. acknowledges support from the European Union's Horizon 2020 research and innovation programme under Grant Agreement No. 763989 APOLO. H.K. acknowledges support from the Digital Research Innovation Institution Program through the National Research Foundation of Korea (NRF) funded by Ministry of Science and ICT (RS-2023-00283597).

Conflict of Interest

The authors declare no conflict of interest.

Author Contributions

H.K. and J.-M.H. contributed equally to this work.

Data Availability Statement

The data that support the findings of this study are available from the corresponding author upon reasonable request.

Keywords

defect passivation, interface engineering, MAPbBr₃, perovskite light-emitting diodes, thiol additive

Received: June 27, 2024
Revised: September 8, 2024
Published online:

- [1] J. S. Kim, J.-M. Heo, G.-S. Park, S.-J. Woo, C. Cho, H. J. Yun, D.-H. Kim, J. Park, S.-C. Lee, S.-H. Park, E. Yoon, N. C. Greenham, T.-W. Lee, *Nature*. **2022**, 611, 688.
- [2] a) L. N. Quan, B. P. Rand, R. H. Friend, S. G. Mhaisalkar, T.-W. Lee, E. H. Sargent, *Chem. Rev.* **2019**, 119, 7444; b) T.-H. Han, K. Y. Jang, Y. Dong, R. H. Friend, E. H. Sargent, T.-W. Lee, *Nature Rev. Mater.* **2022**, 7, 757.
- [3] G. Xing, B. Wu, X. Wu, M. Li, B. Du, Q. Wei, J. Guo, E. K. L. Yeow, T. C. Sum, W. Huang, *Nat. Commun.* **2017**, 8, 14558.
- [4] V. D'Innocenzo, G. Grancini, M. J. P. Alcocer, A. R. S. Kandada, S. D. Stranks, M. M. Lee, G. Lanzani, H. J. Snaith, A. Petrozza, *Nat. Commun.* **2014**, 5, 3586.
- [5] H. He, Q. Yu, H. Li, J. Li, J. Si, Y. Jin, N. Wang, J. Wang, J. He, X. Wang, Y. Zhang, Z. Ye, *Nat. Commun.* **2016**, 7, 10896.
- [6] Q. Zhou, Z. Bai, W. Lu, Y. Wang, B. Zou, H. Zhong, *Adv. Mater.* **2016**, 28, 9163.
- [7] H. Huang, Q. Xue, B. Chen, Y. Xiong, J. Schneider, C. Zhi, H. Zhong, A. L. Rogach, *Angew. Chem., Int. Ed.* **2017**, 56, 9571.
- [8] H. Huang, M. I. Bodnarchuk, S. V. Kershaw, M. V. Kovalenko, A. L. Rogach, *ACS Energy Lett.* **2017**, 2, 2071.
- [9] Y.-H. Kim, S. Kim, A. Kakekhani, J. Park, J. Park, Y.-H. Lee, H. Xu, S. Nagane, R. B. Wexler, D.-H. Kim, S. H. Jo, L. Martinez-Sarti, P. Tan, A. Sadhanala, G.-S. Park, Y.-W. Kim, B. Hu, H. J. Bolink, S. Yoo, R. H. Friend, A. M. Rappe, T.-W. Lee, *Nat. Photonics* **2021**, 15, 148.
- [10] Y. Jiang, M. Cui, S. Li, C. Sun, Y. Huang, J. Wei, L. Zhang, M. Lv, C. Qin, Y. Liu, M. Yuan, *Nat. Commun.* **2021**, 12, 336.
- [11] K. Lin, J. Xing, L. N. Quan, F. P. G. de Arquer, X. Gong, J. Lu, L. Xie, W. Zhao, D. Zhang, C. Yan, W. Li, X. Liu, Y. Lu, J. Kirman, E. H. Sargent, Q. Xiong, Z. Wei, *Nature*. **2018**, 562, 245.
- [12] Z. Fang, W. Chen, Y. Shi, J. Zhao, S. Chu, J. Zhang, Z. Xiao, *Adv. Funct. Mater.* **2020**, 30, 1909754.
- [13] T. Chiba, Y. Hayashi, H. Ebe, K. Hoshi, J. Sato, S. Sato, Y.-J. Pu, S. Ohisa, J. Kido, *Nat. Photonics*. **2018**, 12, 681.
- [14] Y. Hassan, J. H. Park, M. L. Crawford, A. Sadhanala, J. Lee, J. C. Sadighian, E. Mosconi, R. Shivanna, E. Radicchi, M. Jeong, C. Yang, H. Choi, S. H. Park, M. H. Song, F. De Angelis, C. Y. Wong, R. H. Friend, B. R. Lee, H. J. Snaith, *Nature*. **2021**, 591, 72.
- [15] B. Zhao, S. Bai, V. Kim, R. Lamboll, R. Shivanna, F. Auras, J. M. Richter, L. Yang, L. Dai, M. Alsari, X.-J. She, L. Liang, J. Zhang, S. Lilliu, P. Gao, H. J. Snaith, J. Wang, N. C. Greenham, R. H. Friend, D. Di, *Nat. Photonics*. **2018**, 12, 783.
- [16] M. Vasilopoulou, A. Fakharuddin, F. P. García de Arquer, D. G. Georgiadou, H. Kim, A. R. bin Mohd Yusoff, F. Gao, M. K. Nazeeruddin, H. J. Bolink, E. H. Sargent, *Nat. Photon.* **2021**, 15, 656.
- [17] X. Zhao, Z.-K. Tan, *Nat. Photonics*. **2020**, 14, 215.
- [18] Y. Cao, N. Wang, H. Tian, J. Guo, Y. Wei, H. Chen, Y. Miao, W. Zou, K. Pan, Y. He, H. Cao, Y. Ke, M. Xu, Y. Wang, M. Yang, K. Du, Z. Fu, D. Kong, D. Dai, Y. Jin, G. Li, H. Li, Q. Peng, J. Wang, W. Huang, *Nature*. **2018**, 562, 249.
- [19] H. Cho, S.-H. Jeong, M.-H. Park, Y.-H. Kim, C. Wolf, C.-L. Lee, J. H. Heo, A. Sadhanala, N. Myoung, S. Yoo, S. H. Im, R. H. Friend, T.-W. Lee, *Science*. **2015**, 350, 1222.
- [20] L. K. Ono, S. (Frank) Liu, Y. Qi, *Angew. Chem., Int. Ed.* **2020**, 59, 6676.
- [21] Y. Zhou, I. Poli, D. Meggiolaro, F. De Angelis, A. Petrozza, *Nat. Rev. Mater.* **2021**, 6, 986.
- [22] S.-J. Woo, J. S. Kim, T.-W. Lee, *Nat. Photon.* **2021**, 15, 630.
- [23] M.-H. Park, J. S. Kim, J.-M. Heo, S. Ahn, S.-H. Jeong, T.-W. Lee, *ACS Energy Lett.* **2019**, 4, 1134.
- [24] B. Chen, P. N. Rudd, S. Yang, Y. Yuan, J. Huang, *Chem. Soc. Rev.* **2019**, 48, 3842.
- [25] M. Lai, A. Obliger, D. Lu, C. S. Kley, C. G. Bischak, Q. Kong, T. Lei, L. Dou, N. S. Ginsberg, D. T. Limmer, P. Yang, *Proc. Natl. Acad. Sci. USA*. **2018**, 115, 11929.
- [26] Y. Yuan, J. Huang, *Acc. Chem. Res.* **2016**, 49, 286.
- [27] C. Eames, J. M. Frost, P. R. F. Barnes, B. C. O'Regan, A. Walsh, M. S. Islam, *Nat. Commun.* **2015**, 6, 7497.
- [28] H. Kim, J. S. Kim, J.-M. Heo, M. Pei, I.-H. Park, Z. Liu, H. J. Yun, M.-H. Park, S.-H. Jeong, Y.-H. Kim, J.-W. Park, E. Oveisi, S. Nagane, A. Sadhanala, L. Zhang, J. J. Kweon, S. K. Lee, H. Yang, H. M. Jang, R. H. Friend, K. P. Loh, M. K. Nazeeruddin, N.-G. Park, T.-W. Lee, *Nat. Commun.* **2020**, 11, 3378.
- [29] Z. Chu, Q. Ye, Y. Zhao, F. Ma, Z. Yin, X. Zhang, J. You, *Adv. Mater.* **2021**, 33, 2007169.

- [30] A. Liang, K. Wang, Y. Gao, B. P. Finkenauer, C. Zhu, L. Jin, L. Huang, L. Dou, *Angew. Chem., Int. Ed.* **2021**, *60*, 8337.
- [31] Y. Liu, Z. Yu, S. Chen, J. H. Park, E. D. Jung, S. Lee, K. Kang, S.-J. Ko, J. Lim, M. H. Song, B. Xu, H. J. Snaith, S. H. Park, B. R. Lee, *Nano Energy* **2021**, *80*, 105511.
- [32] N. K. Noel, A. Abate, S. D. Stranks, E. S. Parrott, V. M. Burlakov, A. Goriely, H. J. Snaith, *ACS Nano* **2014**, *8*, 9815.
- [33] X. Yang, X. Zhang, J. Deng, Z. Chu, Q. Jiang, J. Meng, P. Wang, L. Zhang, Z. Yin, J. You, *Nat. Commun.* **2018**, *9*, 570.
- [34] A. A. Sutanto, C. Igci, H. Kim, H. Kanda, N. Shibayama, M. Mensi, V. I. E. Queloz, C. Momblona, H. J. Yun, H. J. Bolink, A. J. Huckaba, M. K. Nazeeruddin, *ACS Appl. Energy Mater.* **2021**, *4*, 1259.
- [35] Y.-H. Kim, H. Cho, J. H. Heo, T.-S. Kim, N. Myoung, C.-L. Lee, S. H. Im, T.-W. Lee, *Adv. Mater.* **2015**, *27*, 1248.
- [36] W. T. M. Van Gompel, R. Herckens, G. Reekmans, B. Ruttens, J. D'Haen, P. Adriaensens, L. Lutsen, D. Vanderzande, *J. Phys. Chem. C* **2018**, *122*, 4117.
- [37] M.-H. Park, S.-H. Jeong, H.-K. Seo, C. Wolf, Y.-H. Kim, H. Kim, J. Byun, J. S. Kim, H. Cho, T.-W. Lee, *Nano Energy* **2017**, *42*, 157.
- [38] Y.-H. Kim, G.-H. Lee, Y.-T. Kim, C. Wolf, H. J. Yun, W. Kwon, C. G. Park, T.-W. Lee, *Nano Energy* **2017**, *38*, 51.
- [39] N. Kubota, J. W. Mullin, *J. Cryst. Growth* **1995**, *152*, 203.
- [40] J. He, J. Liu, Y. Hou, Y. Wang, S. Yang, H. G. Yang, *Nat. Commun.* **2020**, *11*, 4237.
- [41] P. Du, J. Li, L. Wang, L. Sun, X. Wang, X. Xu, L. Yang, J. Pang, W. Liang, J. Luo, Y. Ma, J. Tang, *Nat. Commun.* **2021**, *12*, 4751.
- [42] G. Xing, M. H. Kumar, W. K. Chong, X. Liu, Y. Cai, H. Ding, M. Asta, M. Grätzel, S. Mhaisalkar, N. Mathews, T. C. Sum, *Adv. Mater.* **2016**, *28*, 8191.
- [43] T. Schmidt, K. Lischka, W. Zulehner, *Phys. Rev. B* **1992**, *45*, 8989.
- [44] T. Gershon, B. Shin, N. Bojarczuk, T. Gokmen, S. Lu, S. Guha, *J. Appl. Phys.* **2013**, *114*, 154905.
- [45] S.-H. Jeong, S.-H. Woo, T.-H. Han, M.-H. Park, H. Cho, Y.-H. Kim, H. Cho, H. Kim, S. Yoo, T.-W. Lee, *NPG Asia Mater.* **2017**, *9*, e411.
- [46] S.-H. Jeong, J. Park, T.-H. Han, F. Zhang, K. Zhu, J. S. Kim, M.-H. Park, M. O. Reese, S. Yoo, T.-W. Lee, *Joule* **2020**, *4*, 1206.